Theor. Comput. Fluid Dyn. (2018) 32:425–449
https://doi.org/10.1007/s00162-018-0461-5

ORIGINAL ARTICLE

Ramesh Bhoraniya · Narayanan Vinod

Global stability analysis of axisymmetric boundary layer over a circular cylinder

Received: 20 July 2016 / Accepted: 16 April 2018 / Published online: 2 May 2018

Abstract This paper presents a linear global stability analysis of the incompressible axisymmetric boundary layer on a circular cylinder. The base flow is parallel to the axis of the cylinder at inflow boundary. The pressure gradient is zero in the streamwise direction. The base flow velocity profile is fully non-parallel and non-similar in nature. The boundary layer grows continuously in the spatial directions. Linearized Navier–Stokes (LNS) equations are derived for the disturbance flow quantities in the cylindrical polar coordinates. The LNS equations along with homogeneous boundary conditions forms a generalized eigenvalues problem. Since the base flow is axisymmetric, the disturbances are periodic in azimuthal direction. Chebyshev spectral collocation method and Arnoldi's iterative algorithm is used for the solution of the general eigenvalues problem. The global temporal modes are computed for the range of Reynolds numbers and different azimuthal wave numbers. The largest imaginary part of the computed eigenmodes is negative, and hence, the flow is temporally stable. The spatial structure of the eigenmodes shows that the disturbance amplitudes grow in size and magnitude while they are moving towards downstream. The global modes of axisymmetric boundary layer are more stable than that of 2D flat-plate boundary layer at low Reynolds number. However, at higher Reynolds number they approach 2D flat-plate boundary layer. Thus, the damping effect of transverse curvature is significant at low Reynolds number. The wave-like nature of the disturbance amplitudes is found in the streamwise direction for the least stable eigenmodes.

Keywords Axisymmetric boundary layer · Global stability · Transverse curvature

1 Introduction

The linear stability analysis with the parallel base flow assumption is termed as local stability analysis where the base flow is varying only in wall normal direction. The linear stability of shear flows is governed by classical Orr–Sommerfeld equation. The numerical solution to such problems deals with solutions of Orr–Sommerfeld equation obtained for disturbance amplitude functions which are of wave-like nature. It is assumed that streamwise wave number is constant at each streamwise location and disturbance amplitude functions are a function of wall normal coordinate only. The numerical solution of Orr–Sommerfeld equation for parallel base flow assumption can be achieved with very limited computational efforts [7]. The numerical solutions of Orr–Sommerfeld equation obtained for disturbance amplitude functions are of wave-like nature. It is assumed

---

Communicated by Vassilios Theofilis.

R. Bhoraniya · N. Vinod (✉)
Department of Mechanical Engineering, Indian Institute of Technology, Gandhinagar, India
E-mail: vinod@iitgn.ac.in

R. Bhoraniya
E-mail: rameshbhoraniya@iitgn.ac.in

that streamwise wave number is constant at each streamwise location and disturbance amplitude functions are a function of wall normal coordinate only. In spatially growing boundary layers, the base flow velocity is varying in streamwise direction which results in a considerable wall normal velocity. In these cases, non-parallel effects are very strong and cannot be neglected. This is true at low and moderate Reynolds numbers. The parallel flow assumption is not a good approximation for real flows where the flow is varying in streamwise direction. Under such conditions, the flow becomes two-dimensional and only wave-like nature of the solution is not expected. However, it may be one of the solutions. Therefore, stability analysis with the parallel flow assumption may not represent the complete flow physics, and hence, it is having very limited scope for parallel and weakly non-parallel (WNP) flows only.

In the last decade, the stability analysis of non-parallel flow has received much attention through global stability analysis. Here, the base flow is varying in both radial and axial directions. The term global instability is used to represent instability analysis of the such flows [34]. The base flow considered here is non-parallel due to continuous growth of boundary layer in spatial directions and not self-similar due to transverse curvature effect [14,41].

Global temporal modes are time harmonic solutions of the homogeneous linearized disturbance equations with homogeneous boundary conditions in space. Such solutions have been obtained for a base flow with strong non-parallel effects. If the base flow is varying slowly on the scale of a typical instability wavelength, global modes can be recovered by WKBJ type analysis [6]. A boundary layer at high Reynolds numbers and flow through diverging channels at small angles of divergence are common examples of weakly non-parallel flows. The boundary layer at low and moderate Reynolds numbers has strong non-parallel effects, and hence, WKBJ approach may not be the right choice. The prediction by non-parallel theory also agrees better with the experiments at moderate Reynolds numbers.

Joseph [17] is the first among all to introduce the term global stability analysis, where he studied perturbation energy and established lower bounds for flow stability. Bert [3] reported the discovery of short-wavelength elliptic instability in inviscid vortex flows, a problem related to both transition and turbulence research. Bert discovered short-wavelength instability for inviscid vortex flow related to transition and turbulence research [3]. Jackson [16] reports first computations on viscous flow where he studied flow past various shaped bodies. Onset of periodic behaviour in two-dimensional laminar flow past bodies of various shapes is examined by means of finite-element simulations. Zebib [43] studied growth of symmetric and asymmetric perturbations for flow past a circular cylinder. They found that the symmetric disturbances are stable; the asymmetric perturbations become unstable at a Reynolds number about 40 with a Strouhal number about 0.12. Christodoulou [4] used the global approach for free surface flow, Tatsumi [32] for rectangular duct flow and Lin [19] for boundary layer flows. The matrices generated by the discretization of global stability equations are very large, non-symmetric and sparse, which requires significant computational resources. All above-said works have implemented QR algorithm for computations of eigenvalues and eigenvectors of resulting matrices. This algorithm computes all the eigenvalues. However, flow becomes unstable in case of a shear flow due to very few dangerous modes only; it is more economical to calculate that modes only. Iterative techniques like Arnoldi's algorithm with shift-invert strategy compute few selected eigenvalues near the shift value. Theofilis [39] studied 2D steady laminar separation bubble using WNP and DNS and got an excellent agreement of the stability results for both 2D and 3D. By performing a global stability analysis, they proved the existence of new instability modes that are not explored by either of the approaches, i.e. WNP & DNS. Theofilis [34] studied the global stability of separated profiles in three different flow configurations, and they show that the amplitude of the global mode is less in the separated region than in the wake region or shear layer region. Ehrenstein [12] studied the global instability of a flat-plate boundary layer. By an optimal superposition of the global temporal modes, they were able to simulate the convective nature of instability of the boundary layer. Alizard [2] performed a global stability analysis on a flat-plate boundary layer and obtained an excellent agreement with the local stability results and the WNP results. Monokrousos [25] performed a global stability analysis of the flat plate boundary layer and calculated the maximum energy growth with a reduced order model and found that optimal energy growth cannot be obtained with least stable global modes only, but it is necessary to consider few globally stable modes also. This is essential for flow control. Tezuka [33] has first time solved initial value problem based on the same approach for three-dimensional disturbances.

It is interesting to review the literature on the instabilities of axisymmetric boundary layer on a circular cone. Most of the research work done so far is in compressible regime. The stability of supersonic flow past a sharp cone was studied by Mack [21] using linear stability theory. The effect of curvature was neglected in their study. Later Malik and Spall [24] presented the viscous compressible boundary layer equations for an axisymmetric basic flow. The stability analysis was performed for axisymmetric and non-axisymmetric disturbances [24]. In the experimental work on blunt bodies and walls with concave curvature, they considered two-dimensional and three-dimensional disturbances for studying TS and Gortler instabilities. They found that transverse curvature has a stabilizing effect on axisymmetric disturbances and destabilizing effect on non-axisymmetric disturbances. Duck [8] showed that the effect of transverse curvature becomes very small when the radius of the body is much larger than the boundary layer thickness. Duck and Hall [10] later studied the instability of supersonic flow over an axisymmetric boundary layer for two-dimensional and three-dimensional disturbances. They concluded that the neutral stability boundaries show no similarity when the effect of transverse curvature is significant [10]. Duck [9] studied supersonic flow past a straight circular cylinder for axisymmetric mode. He found that as curvature increases, first unstable inviscid mode disappears rapidly and amplification rate of second mode reduces [9]. Duck and Shaw [11] continued this study with non-axisymmetric disturbances for a laminar boundary layer on a sharp cone in supersonic flow and obtained inviscid growth rates. They identified the most unstable disturbances as a new mode of instability waves [11].

The study of stability analysis of incompressible axisymmetric boundary layer is found very sparse in the literature. The available literature on axisymmetric boundary layers is limited to local stability analysis. Rao [28] first studied the stability of axisymmetric boundary layer. He found that non-axisymmetric disturbances are less stable than that of two-dimensional disturbances. The estimated critical Reynolds number based on free-stream velocity and body radius of the cylinder was 11,000. Later work of Tutty [40] investigated that for non-axisymmetric mode critical Reynolds number increases with azimuthal wave number N. The critical Reynolds number found to be 1060 for $N = 1$ mode and 12,439 for $N = 0$ mode. The axisymmetric mode is found least stable fourth mode. Recently, Vinod [41] investigated that higher non-axisymmetric mode $N = 2$ is linearly stable for a small range of curvature only. The helical mode $N = 1$ is unstable over a significant length of the cylinder, but never unstable for curvature above 1. Thus, transverse curvature has overall stabilizing effect over base flow and perturbations. Malik [23] studied the effect of transverse curvature on the stability of incompressible boundary layer. They investigated that the body curvature and streamline curvature are having significant damping effects on disturbances. They also found that travelling waves are the most amplified waves in three-dimensional boundary layers. Vinod and Govindarajan [42] studied secondary instability of an incompressible axisymmetric boundary layer. They found that laminar flow is always stable at high transverse curvature to secondary disturbances.

Petrov [27] is the first to study stability of boundary layer formed on a rotating cylinder. Streamwise velocity profile were obtained for small axial length and show the existence of wall jet effect at large rotation rate. However, this interesting fact was not explained in the paper [27]. Kao and Chao [18] also studied stability analysis for rotating cylinder. However, the centrifugal force term is missing in boundary layer equation and they could not find any wall jet effect even at high rate of rotation. Herrada [15] have obtained stability analysis results for a axisymmetric boundary layer with the rotating cylinder with certain range of rotation rates. They were unable to get any wall jet effect in their study. Muralidhar et al. [26] have obtained stability results for the rotating cylinder with high Reynolds number. They considered Reynolds number and rotational rate as control parameters, and the boundary layer equations used are not limited to the case where boundary layer thickness is thin compared to cylinder radius. At large downstream distance, the flow differs from the Blasius profile due to the effect of curvature and rotation. As rotation rate increases, the centrifugal force increases the radial pressure gradient and wall jet exists. The wall jet effect becomes stronger with the increase in rotation rate. Parallel base flow assumption is considered in all above investigations.

The two-dimensional global modes are computed for the flat-plate boundary layer by some investigators [1,2,12]. However, this is the first attempt to compute global temporal modes for the axisymmetric boundary layer. The main aim of this paper is to study the global stability characteristics of the axisymmetric boundary layer and the effect of transverse curvature on it. The base flow on a circular cylinder is computed with the two different base flow configurations; real boundary layer with spherical cap as shown in Fig. 1 and model boundary layer with assumption that boundary layer directly develops on the cylindrical surface. The instability analysis for real and model axisymmetric boundary layers is studied. The characteristics of the global eigenmodes of axisymmetric boundary layer are compared with the flat-plate boundary layer (with zero transverse curvature) at different Reynolds numbers. The comparison shows that the transverse curvature has overall stabilizing effect on the disturbances.

2 Problem formulation

We follow the standard procedure to derive linearized Navier–Stokes equations for disturbance flow quantities. The Navier–Stokes equations for base flow and instantaneous flow are written in polar cylindrical coordinates

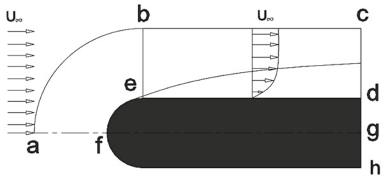

Fig. 1 Schematic diagram of axisymmetric boundary layer on a circular cylinder

(r, θ, x). The equations are non-dimensionalized using free-stream velocity (U_∞) and displacement thickness (δ^*) at the inlet of the domain. Following the standard procedure of stability analysis, we get the set of equations for disturbance flow quantities. The base flow is axisymmetric, and disturbances are three-dimensional in nature. The Reynolds number is defined as,

$$R_e = \frac{U_\infty \delta^*}{\nu} \tag{1}$$

The flow quantities are split into base flow and perturbations,

$$\overline{U} = U + u, \overline{V} = V + v, \overline{W} = 0 + w, \overline{P} = P + p, \tag{2}$$

We assume normal mode form for disturbances with amplitude varying in radial (r) and streamwise (x) directions. It is correct to assume periodicity in the azimuthal (θ) direction as the flow is axisymmetric.

$$\mathbf{q}(x, r, t) = \hat{\mathbf{q}}(x, r)e^{[i(N\theta - \omega t)]} \tag{3}$$

where $\mathbf{q} = [u, v, w, p]$, $\mathbf{Q} = [U, V, W, P]$, $\overline{\mathbf{Q}} = [\overline{U}, \overline{V}, \overline{W}, \overline{P}]$, ω is the frequency of the waves, N is the azimuthal wave number, U_∞ is the free-stream velocity, δ^* is the displacement thickness, a is the body radius of the cylinder, where q, Q and $\overline{Q}$ are the perturbation, base and instantaneous flow quantities, respectively. u, v and w are the disturbance velocity components in the axial (x), radial (r) and azimuthal (θ) directions, respectively. The linearized Navier–Stokes equations for instability analysis are as follows:

$$\frac{\partial u}{\partial t} + U\frac{\partial u}{\partial x} + u\frac{\partial U}{\partial x} + V\frac{\partial u}{\partial r} + v\frac{\partial U}{\partial r} + \frac{\partial p}{\partial x} - \frac{1}{Re}[\nabla^2 u] = 0 \tag{4}$$

$$\frac{\partial v}{\partial t} + U\frac{\partial v}{\partial x} + u\frac{\partial V}{\partial x} + V\frac{\partial v}{\partial r} + v\frac{\partial V}{\partial r} + \frac{\partial p}{\partial r} - \frac{1}{Re}\left[\nabla^2 v - \frac{v}{r^2} - \frac{2}{r^2}\frac{\partial w}{\partial \theta}\right] = 0 \tag{5}$$

$$\frac{\partial w}{\partial t} + U\frac{\partial w}{\partial x} + V\frac{\partial w}{\partial r} + V\frac{w}{r} + \frac{1}{r}\frac{\partial p}{\partial \theta} - \frac{1}{Re}\left[\nabla^2 w - \frac{w}{r^2} + \frac{2}{r^2}\frac{\partial v}{\partial \theta}\right] = 0 \tag{6}$$

$$\frac{\partial u}{\partial x} + \frac{\partial v}{\partial r} + \frac{v}{r} + \frac{1}{r}\frac{\partial w}{\partial \theta} = 0 \tag{7}$$

where

$$\nabla^2 = \frac{\partial^2}{\partial x^2} + \frac{\partial^2}{\partial r^2} + \frac{1}{r}\frac{\partial}{\partial r} + \frac{1}{r^2}\frac{\partial^2}{\partial \theta^2} = 0 \tag{8}$$

2.1 Boundary conditions

At wall, on the solid surface of cylinder, no-slip and no-penetration boundary conditions are applied. All disturbance velocity components have zero magnitude at the solid surface of the cylinder.

$$u(x, a) = 0,\ v(x, a) = 0,\ w(x, a) = 0 \tag{9}$$

At free stream far away from the surface of cylinder, exponential decay of disturbances is expected. Homogeneous Dirichlet boundary conditions are applied for velocity and pressure disturbances at free stream.

$$u(x, \infty) = 0,\ v(x, \infty) = 0,\ w(x, \infty) = 0,\ p(x, \infty) = 0 \tag{10}$$

The boundary conditions in streamwise direction are not straight forward. Homogeneous Dirichlet boundary conditions are applied on disturbance velocity components at the inlet. This boundary condition is appropriate as suggested by Theofilis [34] because we are interested in the disturbances evolved within the basic flow field only. At outlet, one may apply boundary conditions based on the incoming/outgoing wave information [13]. Such conditions impose wave-like nature of the disturbances, and it is more restrictive in nature. This is not appropriate from the physical point of view in instability analysis. Even the wave number α is not known initially in case of a global stability analysis. An alternative way is to impose numerical boundary condition which extrapolates information from the interior of the computational domain. Linear extrapolated conditions are applied by several investigators. Review of the literature on global stability analysis suggests linearly extrapolated boundary conditions are the good approximations [31,34]. We also tried second-order extrapolated boundary conditions; however, the difference is only marginal. Thus, we considered linear extrapolated conditions at outflow boundary.

$$u(x_{in}, r) = 0, \ v(x_{in}, r) = 0, \ w(x_{in}, r) = 0, \tag{11}$$

$$u_{n-2}[x_n - x_{n-1}] - u_{n-1}[x_n - x_{n-2}] + u_n[x_{n-1} - x_{n-2}] = 0 \tag{12}$$

Similarly, one can write extrapolated boundary conditions for wall normal and azimuthal disturbance components v and w, respectively. The boundary conditions for pressure do not exist physically at the wall. However, compatibility conditions derived from the linearized Navier–Stokes equations are collocated at the wall of cylinder [34].

$$\frac{\partial p}{\partial x} = \frac{1}{Re}[\bigtriangledown^2 u] - U\frac{\partial u}{\partial x} - V\frac{\partial u}{\partial r} \tag{13a}$$

$$\frac{\partial p}{\partial r} = \frac{1}{Re}[\bigtriangledown^2 v] - U\frac{\partial v}{\partial x} - V\frac{\partial v}{\partial r} \tag{13b}$$

The linearized Navier–Stokes equations are discretized using Chebyshev spectral collocation method. The Chebyshev polynomial generates non-uniform grids and generates more collocation points towards the ends. It is a favourable arrangement for the boundary value problems.

$$x_{\text{cheb}} = \cos\left(\frac{\pi i}{n}\right) \quad \text{where} \quad i = 0, 1, 2, 3 \ldots n \tag{14}$$

$$y_{\text{cheb}} = \cos\left(\frac{\pi j}{m}\right) \quad \text{where} \quad j = 0, 1, 2, 3 \ldots m \tag{15}$$

where n and m are number of collocation points in streamwise and wall normal direction. The gradient of disturbance amplitude functions is very large near the wall region within the thin boundary layer, which requires a large number of grid points to increase the spatial resolution. Grid stretching is applied via the following algebraic equation [22].

$$y_{\text{real}} = \frac{y_i L_y (1 - y_{\text{cheb}})}{L_y + y_{\text{cheb}}(L_y - 2y_i)} + a \tag{16}$$

In the above grid stretching method, a half number of the collocation points are concentrated within the y_i distance from the lower boundary only. The non-uniform nature of distribution for collocation points in the streamwise direction is undesirable. The maximum and minimum distances between the grid points are at centre and end, respectively. Thus, it makes a poor resolution at the centre of the domain and a very small distance between the grids at the end gives rise to Gibbs phenomenon. To improve the resolution and to minimize the Gibbs oscillation in the solution, grid mapping is implemented in streamwise direction using following algebraic equation [5].

$$x_{\text{map}} = \frac{\sin^{-1}(\alpha_m x_{\text{cheb}})}{\sin^{-1}(\alpha_m)} \tag{17}$$

The value of α_m is selected carefully to improve spatial resolution in the streamwise direction. A very small value of α_m keeps the grid distribution like Chebyshev and near to unity almost uniform grid. For the detail description of the grid mapping, readers are suggested to refer [5]. To incorporate the effect of physical dimensions of the domain $[L_x, L_y]$ along with grid stretching and mapping, it is required to multiply the Chebyshev differentiation matrices by proper Jacobean matrix. Once all the partial derivatives of the LNS are discretized by spectral collocation method using Chebyshev polynomials, the operator of the differential equations formulates the matrices A and B. These matrices are square, real and sparse in nature, and formulate general eigenvalues problem.

$$\begin{bmatrix} A_{11} & A_{12} & A_{13} & A_{14} \\ A_{21} & A_{22} & A_{23} & A_{24} \\ A_{31} & A_{32} & A_{33} & A_{34} \\ A_{41} & A_{42} & A_{43} & A_{44} \end{bmatrix} \begin{bmatrix} u \\ v \\ w \\ p \end{bmatrix} = i\omega \begin{bmatrix} B_{11} & B_{12} & B_{13} & B_{14} \\ B_{21} & B_{22} & B_{23} & B_{24} \\ B_{31} & B_{32} & B_{33} & B_{34} \\ B_{41} & B_{42} & B_{43} & B_{44} \end{bmatrix} \begin{bmatrix} u \\ v \\ w \\ p \end{bmatrix} \tag{18}$$

$$[A][\phi] = i\omega[B][\phi]$$

where A and B are square matrix of size $4 \times n \times m$, $i\omega$ is an eigenvalues, and ϕ is a vector of unknown amplitude of disturbance flow quantities u, v, w and p. The above-mentioned all the boundary conditions are properly incorporated in the matrix A and B.

2.2 Solution of general eigenvalues problem

The matrices A and B are sparse in nature and of very large size. For $n = 121$ and $m = 121$, the number of eigenvalues is 58,564., i.e. in the order of (10^4 to 10^5). The eigenvalues problems are very large to solve for all the eigenvalues. However, for instability analysis, the few eigenvalues with its largest imaginary parts, which makes the flow temporally unstable, are important. Hence, we are interested in the few eigenvalues and corresponding eigenvectors only. The QZ algorithm computes the full spectrum of eigenvalues and hence obviously it is not economical. The iterative method based on Arnoldi's algorithm is a proper choice. The Krylov subspace provides the possibility of extracting major part of the spectrum using shift and invert strategy. The computations of Krylov subspace along with Arnoldi's algorithm applied to eigenvalues problem become easy.

$$(A - \lambda B)^{-1} B\phi = \mu\phi \quad \text{where} \quad \mu = \frac{1}{i\omega - \lambda} \tag{19}$$

where λ is the shift parameter and μ is the eigenvalues of the converted problem. Sometimes, it is also called spectral transformation, which converts generalized eigenvalues problem to standard eigenvalues problem. The Krylov subspace may be computed by successive resolution of the linear system with matrix $(A - \lambda B)$, using LU decomposition. Full spectrum method is employed for this small subspace to get a good approximate solution to the original general eigenvalues problem [35]. The large size of the Krylov subspace extracts major part of the spectrum. Generally, the computed spectrum is always nearby the shift parameter. The good approximation of shift parameter reduces the number of iterations to converge the solution to required accuracy level. However, larger size of subspace makes the solution almost independent from the shift parameter λ. We tested the code for several values of shift parameter λ. The convergence of the solution depends on the value of shift parameter. The good approximation of the shift value needs less number of iterations. However, we have taken the maximum number of iterations equal to 300; hence, convergence of the solution may not be affected by shift parameter. Given the large subspace size of $k = 250$, the part of the spectrum for our instability analysis could be recovered in the one computation that took about 2.36 h on Intel Xenon(R) CPU E5 26500@2.00 GHz × 18.

3 Base flow solution

The base flow velocity profile is obtained by solving the steady Navier–Stokes equations (20)–(22) with the finite-volume code Ansys Fluent. The axisymmetric domain is considered with 20 and 200 radius in radial and axial directions as shown in Fig. 1.

$$U\frac{\partial U}{\partial x} + V\frac{\partial U}{\partial r} = -\frac{\partial P}{\partial x} + \frac{1}{R_e}\left(\frac{\partial^2 U}{\partial x^2} + \frac{1}{r}\frac{\partial U}{\partial r} + \frac{\partial^2 U}{\partial r^2}\right) \tag{20}$$

Table 1 The grid convergence study for the base flow is obtained, using $U(x = 75, r = 1.2)$ and $V(x = 75, r = 1.2)$ for $Re = 1000$

Mesh	Grid size	U	ϵ (%)	GCI (%)	V	ϵ (%)	GCI (%)
#1	1001× 251	0.0325125	0.0114	0.0253	1.43466×10^{-5}	0.026	0.0773
#2	708 × 177	0.0325088	0.0268	0.1085	1.43503×10^{-5}	0.055	0.1415
#3	501 × 125	0.0325001	–	–	1.43582×10^{-5}	–	–

The grid refinement ratio (α) in each direction is 1.4142. The relative error (ϵ) and Grid Convergence Index (GCI) are calculated using two consecutive grid size. The j and $j + 1$ represent coarse and fine grids, respectively. $\epsilon = \frac{f_j - f_{j+1}}{f_j} \times 100$. $GCI(\%) = 3[\frac{f_j - f_{j+1}}{f_{j+1}(\alpha^n - 1)}] \times 100$, where n = $\log[\frac{f_j - f_{J+1}}{f_{j+1} - f_{j+2}}]/\log(\alpha)$

$$U\frac{\partial V}{\partial x} + V\frac{\partial V}{\partial r} = -\frac{\partial P}{\partial r} + \frac{1}{R_e}\left(\frac{\partial^2 V}{\partial x^2} + \frac{1}{r}\frac{\partial V}{\partial r} + \frac{\partial^2 V}{\partial r^2}\right) \tag{21}$$

$$\frac{\partial U}{\partial x} + \frac{\partial V}{\partial r} + \frac{V}{r} = 0 \tag{22}$$

Appropriate boundary conditions are applied to close the formulation of the above problem. Uniform streamwise velocity U_∞ was imposed at the inlet and no-slip and no-penetration boundary conditions at the surface of the cylinder. Slip boundary condition ($\mathbf{n}.\mathbf{U} = 0$) was imposed at free stream far away from the solid surface (bc), and outflow boundary conditions at outlet (cd), that consists $\frac{\partial U}{\partial x} = 0$, $\frac{\partial V}{\partial x} = 0$ and $P = 0$. Line afg is the axis of the cylinder. The steady Navier–Stokes equations were solved using SIMPLE algorithm with under-relaxation, to get a stable solution. Quick, a weighted average of second-order upwind and second-order central scheme was used for spatial discretization of momentum equations. Thus, obtained base flow velocity profile is interpolated to spectral grids using cubic spline interpolation to perform global stability analysis. The solution for the base flow has converged with the total 251,251 number of grid points with 1001 and 251 grids in streamwise and radial directions, respectively. The distribution of the grids is geometric in both the directions. We started simulation initially with coarse grid size of 501 and 125 grids in axial and radial directions and refined it with a factor of 1.4142 in each directions. The discretization error was computed through Grid Convergence Index (GCI) study on three consecutive refined grids [30]. The monotonic convergence is found for all these refined grids. In our problem, we computed error and GCI for two field values $U(x = 75, r = 1.2)$ and $V(x = 75, r = 1.2)$ near the surface of the cylinder, where the gradient of the velocity field is maximum. The GCI and error were computed for three different grids as shown in Table 1. The error between Mesh 1 and Mesh 2 is too small. The GCI has also reduced with the increased spatial resolution. It shows that solution is converging monotonically towards the grid-independent one. Further refinement in the grid will hardly improve the accuracy of the solution while increases the time for the computations. The grid is thoroughly refined near the wall where velocity gradient is very high. The convergence order n for U and V is 2.00, which is in agreement with the second-order discretization scheme used in the finite-volume code Ansys Fluent. A Mesh 1 was checked with domain height of 25 times cylinder radius to study the effect of far-field condition. The percentage error between these two domains heights are within 0.1%. Thus, Mesh 1 was used in all the results presented here in to compute velocity field for the base flow.

The base flow velocity profile is computed for the axisymmetric boundary layer with two different configuration. In the first case, it is assumed that the boundary layer develops directly on the cylindrical surface and domain *afeb* is excluded in the base flow computations. In the second case, the hemispherical cap is considered at the leading edge of the circular cylinder and the domain *afeb* is included in the base flow computations. The second configurations are physically more relevant. The boundary layer starts to develop from the tip of the spherical cap itself. Figure 2a, b shows the contour plot for the base velocity U and V. The transverse curvature δ/a increases, while shape factor (H) reduces in the streamwise direction for a given Reynolds number as shown in Fig. 3a, b, respectively. However, at any given streamwise location, the δ/a reduces and H increases with the increased Reynolds number. Shape factor H is smaller for axisymmetric velocity profile in comparison with the Blasius profile. The comparison of the real and model boundary layers in Fig. 4a, b shows that δ/a is higher and H is lower at any streamwise location for $Re = 2000$. Figures 5 and 6 show the comparison of the radial derivatives ($\frac{\partial U}{\partial r}$) and streamwise derivatives ($\frac{\partial U}{\partial x}$) of the U velocity at three different streamwise locations $x = 13.5$, $x = 50$ and $x = 100$. It is observed that the difference in the derivatives magnitudes reduces as x increases. Thus, the effect of spherical cap in base flow profile is higher towards upstream side. The real boundary layer profile is used in all global stability results reported here.

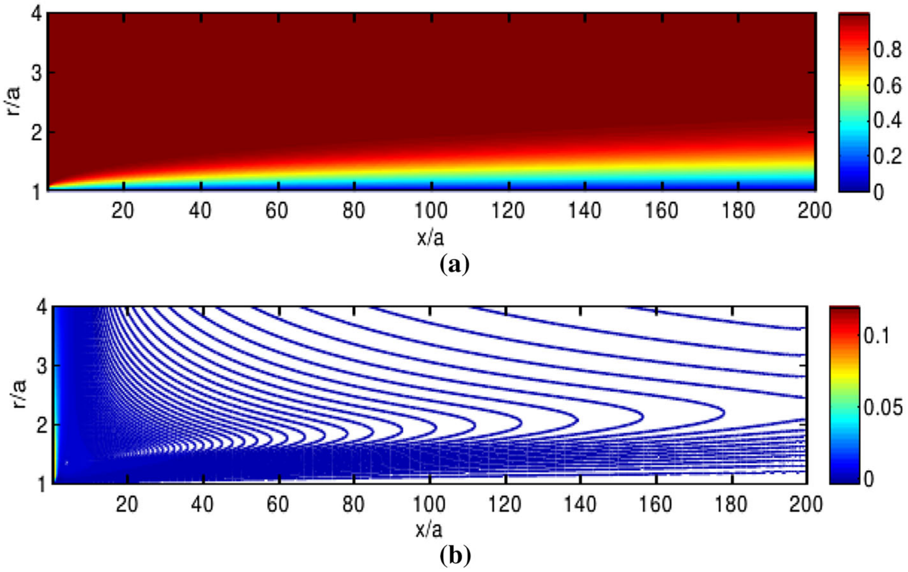

Fig. 2 Base flow velocity profile for **a** Streamwise (U) and **b** Wall normal (V) velocity components for $R_e = 2000$. The Reynolds number is calculated based on body radius of the cylinder. The velocity profile is interpolated to collocation points for instability analysis. The actual domain height in wall normal direction is 20a

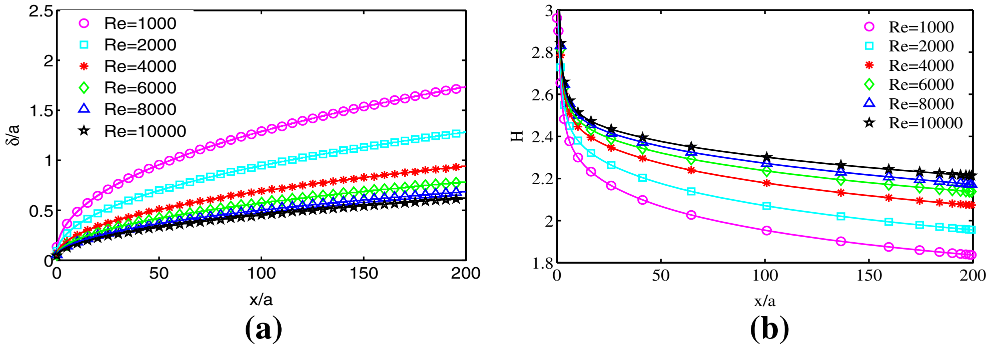

Fig. 3 Variation of **a** transverse curvature (δ/a) and **b** shape factor (H) in the streamwise direction for different Reynolds number. The Reynolds number is based on the body radius of the cylinder. Axial length and radial length are normalized with the cylinder radius

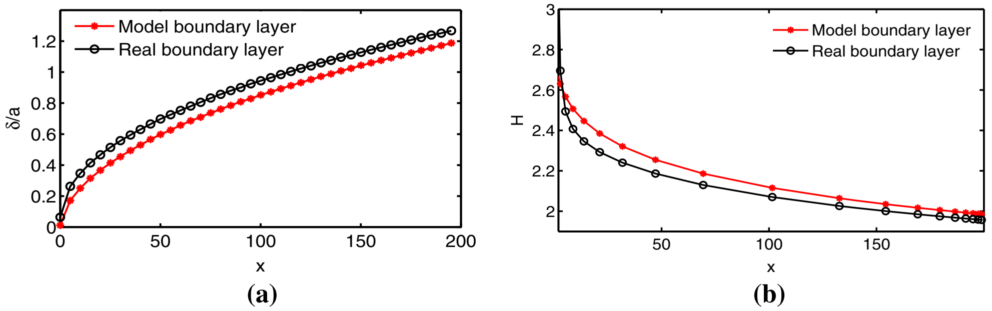

Fig. 4 Comparison of **a** transverse curvature (δ/a) and **b** shape factor (H) in the streamwise direction for real and model axisymmetric boundary layers for $Re = 2000$ based on the radius of the cylinder

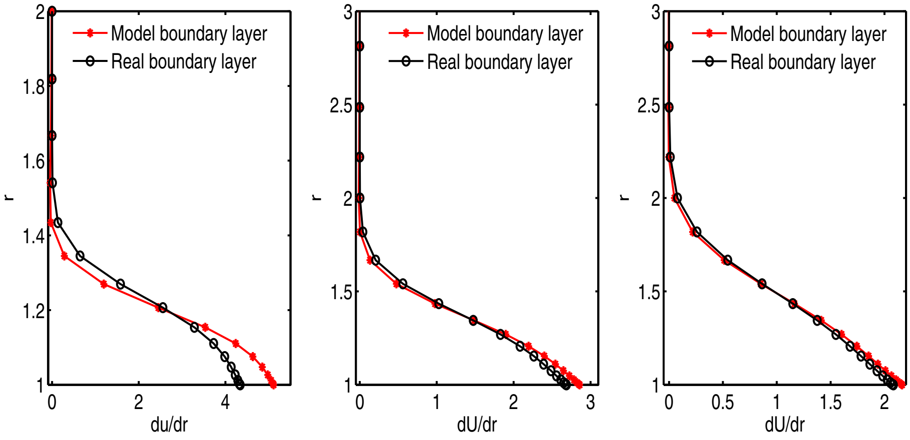

(a) **(b)** **(c)**

Fig. 5 Comparison of $\frac{\partial U}{\partial r}$ at three different streamwise location **a** $x = 13.5$, **b** $x = 50$ and **c** $x = 100$ for real and model axisymmetric boundary layers for $Re = 2000$

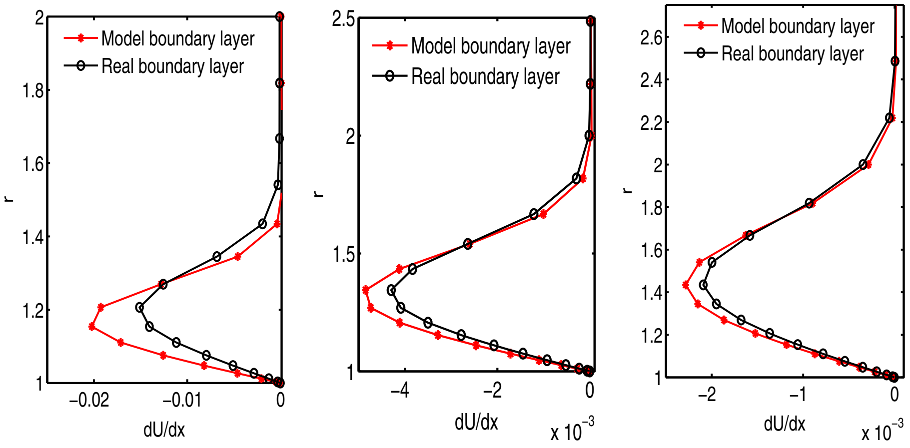

(a) **(b)** **(c)**

Fig. 6 Comparison of $\frac{\partial U}{\partial x}$ at three different streamwise locations **a** $x = 13.5$, **b** $x = 50$ and **c** $x = 100$ for real and model axisymmetric boundary layers for $Re = 2000$

4 Code validation

4.1 Axisymmetric mode ($N = 0$)

For the purpose of preliminary comparisons of global stability results with local stability results, we reduced the global nature of the problem to an equivalent local stability problem. The domain length equal to one wavelength ($L_x = 2\pi/\alpha$) is taken in the streamwise direction for the least stable axisymmetric mode ($N = 0$) and helical mode $N = 1$. Non-parallel effects from the base flow velocity profile are removed to apply parallel flow assumption i. e. $V = 0$ & $\frac{\partial U}{\partial x} = 0$. In the wall normal direction, the boundary conditions are same as that of local stability analysis [34]. To impose wave-like behaviour of disturbances, Robin and periodic boundary conditions are applied in the streamwise direction at inlet and outlet [31]. The Robin boundary conditions with constant streamwise wave number α are prescribed at inlet and outlet. The Robin boundary conditions are derived from the $\phi(r,t) = \hat{\phi}(r)e^{[(i(N\theta-\omega t)]}$. We applied Robin boundary conditions along with periodic boundary conditions at inlet and outlet with constant streamwise wave number α.

$$\frac{\partial^2 u}{\partial x^2} = -\alpha^2 u, \ \frac{\partial^2 v}{\partial x^2} = -\alpha^2 v \tag{23}$$

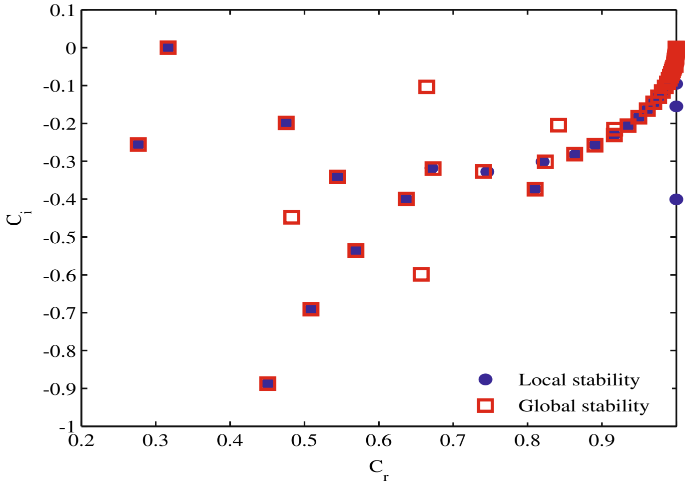

Fig. 7 Comparison of the eigenspectrum of global stability analysis with the local stability analysis of for axisymmetric mode ($N = 0$) and Reynolds number $R_e = 12{,}439$. Here, $R_e = 12{,}439$ is a critical Reynolds number for local stability analysis based on body radius of the cylinder [40]. The critical Re, based on the displacement thickness (δ^*), is 1264

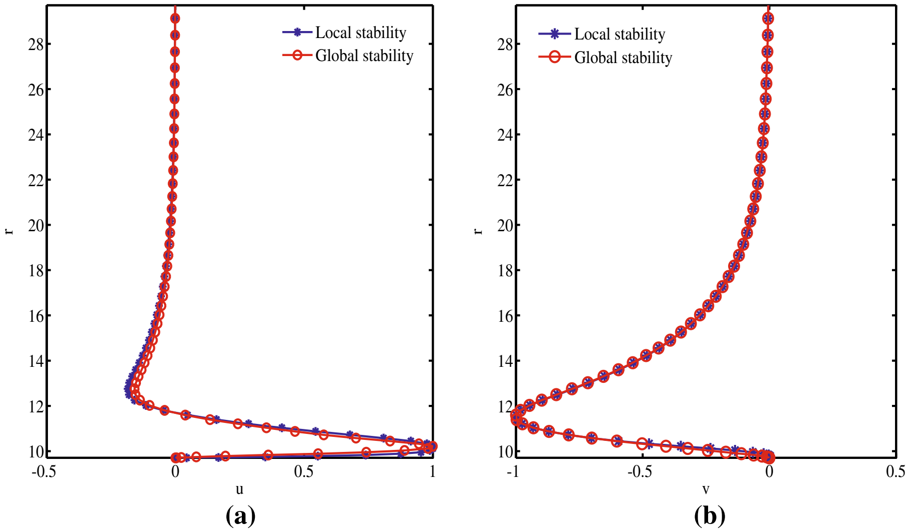

(a) **(b)**

Fig. 8 Comparisons of the real parts of **a** streamwise u and **b** wall normal v eigenfunctions for local and global stability analyses for axisymmetric mode ($N = 0$) for Reynolds number $R_e = 12{,}439$ based on body radius of the cylinder. The Reynolds number based on the displacement thickness (δ^*) is 1264

$$u(x, r) = u(x + L_x, r), v(x, r) = v(x + L_x, r) \tag{24}$$

The above boundary conditions are applied to disturbance velocity components in a streamwise direction at inlet and outlet. The second derivatives are considered to avoid complex quantities in the boundary conditions, and hence, fast computations can take place. Here, we considered axisymmetric mode ($N = 0$) for the validation of global stability results. The critical Reynolds number, streamwise wave number and streamwise location are 12,439, 2.73 and 47, respectively, [40]. The Reynolds number is based on the body radius of the cylinder. Streamwise domain length is taken equal to one wavelength ($L_x = 2.3015$). The domain in streamwise direction is very limited, and hence, the solution is converged with the number of collocation points $n = 41$ in streamwise direction and $m = 101$ in the radial direction. The eigenspectrum and eigenfunctions are in good agreement with the results of local stability analysis of Tutty [40] as shown in Figs. 7 and 8. The streamwise wave number α is computed from the eigenfunctions obtained through global stability analysis, and it is equal to 2.73. Hence, the applied value of α is recovered in the global stability analysis. The perturbation for the

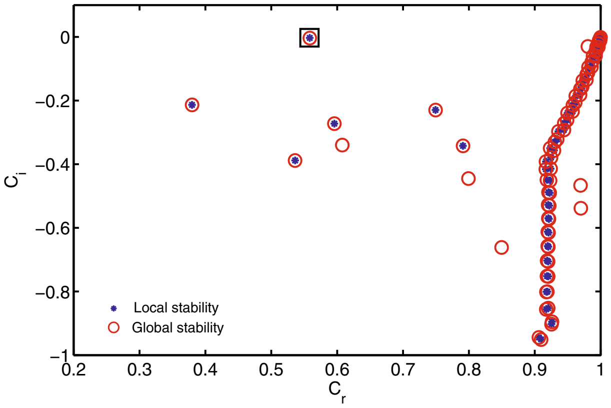

Fig. 9 Comparison of eigenspectrum of global stability analysis with the local stability analysis for helical mode $N = 1$ and Reynolds number $Re = 1060$. Here, $Re = 1060$ is the critical Reynolds number for local stability analysis based on body radius of the cylinder. The critical Re, based on the displacement thickness, is 1020

disturbances u and v can be written as $u(x, r, t) = \hat{u}(x, r)e^{[i\theta_u(x,r)]}$ and, $v(x, r, t) = \hat{v}(x, r)e^{[i\theta_v(x,r)]}$, where θ_u and θ_v are phase angles of wave with respect to x and r. The phase angles of waves can be defined by the following relationship [2].

$$\theta_u = \tan^{-1}\left(\frac{u_i}{u_r}\right), \theta_v = \tan^{-1}\left(\frac{v_i}{v_r}\right) \tag{25}$$

where r and i denotes real and imaginary parts of the eigenfunctions u and v. The phase is dependent on the normal coordinate only. Thus, the position of maximum absolute magnitude of each disturbances remains same at all the streamwise locations. The streamwise wave number (α_r) and spatial growth rate (α_i) are calculated by the following formulas [2].

$$\alpha_{ru} = \frac{\partial\theta_u(x, y_{u_{\max}})}{\partial x}, \alpha_{rv} = \frac{\partial\theta_v(x, y_{v_{\max}})}{\partial x} \tag{26}$$

The amplification rate (A) in the streamwise direction is defined as

$$A(x) = |u(x, y_{u_{\max}})|, A(x) = |v(x, y_{u_{\max}})| \tag{27}$$

The spatial growth rate $-\alpha_i$ is determined from the following formula

$$\alpha_i = -\frac{1}{A}\frac{dA}{dx} \tag{28}$$

4.2 Helical mode ($N = 1$)

The same method is adopted to validate the results of global stability analysis for helical mode $N = 1$. The critical Reynolds number, streamwise wave number and streamwise location for helical mode $N = 1$ are 1060, 0.125 and 543, respectively, [40]. Here, the disturbance velocity components are three-dimensional. The following boundary conditions are considered at inlet and outlet for disturbance velocity components.

$$\frac{\partial^2 u}{\partial x^2} = -\alpha^2 u, \quad \frac{\partial^2 v}{\partial x^2} = -\alpha^2 v, \quad \frac{\partial^2 w}{\partial x^2} = -\alpha^2 w \tag{29}$$

$$u(x, r) = u(x + L_x, r), \quad v(x, r) = v(x + L_x, r), \quad w(x, r) = w(x + L_x, r) \tag{30}$$

Figures 9 and 10 show the comparison of the eigenspectrum and eigenfunctions for the helical mode $N = 1$ for local and global stability analyses. The results of global stability analysis are in good agreement with the local stability analysis.

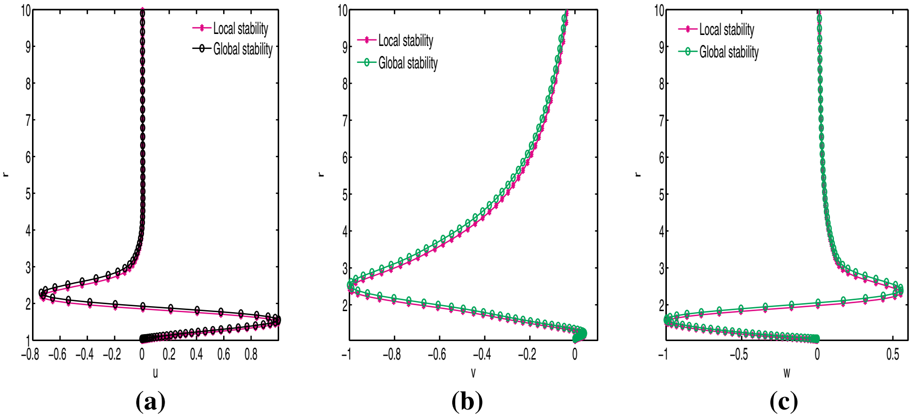

Fig. 10 Comparisons of the real parts of **a** streamwise u and **b** wall normal v and **c** azimuthal w eigenfunctions for local and global stability analyses for axisymmetric mode ($N = 1$) for Reynolds number $R_e = 1060$ based on body radius of the cylinder. The Reynolds number based on the displacement thickness (δ^*) is 1020

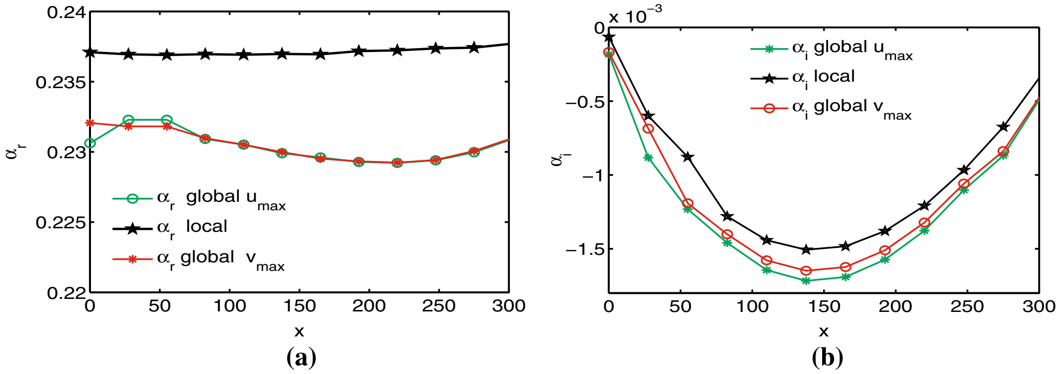

Fig. 11 Comparison of the **a** streamwise wave number α_r and **b** spatial growth rate α_i computed from the eigenfunctions for global and local stability analyses. The associated real frequency $\omega_r = 0.075$

5 Comparison with the local stability analysis

To validate the global stability analysis code, the wave-like nature of the disturbances is imposed at inlet and outlet by Robin boundary conditions. As discussed earlier, it is very restrictive in nature which is not physically more relevant. The streamwise wave number (α_r) and spatial growth rate ($-\alpha_i$) are computed for $x/a = 31$ to $x/a = 54$ using local spatial stability and global stability analyses for the pulsation $\omega_r = 0.075$. The Reynolds number based on the radius of the cylinder is $Re_a = 15{,}000$ ($Re_{\delta^*} = 1141$). Dirichlet and extrapolated boundary conditions are considered at inlet and outlet for global stability analysis as suggested by Theofilis [34]. As shown in Figs. 11 and 12, the computed α_r, α_i and eigenfunctions are in good agreement.

6 Results and discussion

In the present analysis, Reynolds number is varying from 261 to 693 with azimuthal wave numbers 0, 1, 2, 3, 4 and 5. Reynolds number based on the displacement thickness (δ^*) at the inlet of domain is considered. The streamwise and wall normal lengths are normalized with the displacement thickness at the inflow boundary of the domain. The streamwise domain length $L_x = 345$ and wall normal height $L_r = 20$ are selected for the instability analysis. The number of collocation points considered is $n = 121$ in streamwise direction and $m = 121$ in wall normal direction. The general eigenvalues problem is solved using ARPACK, which uses Arnoldi's algorithm. The computed eigenvalues are found to be accurate up to three decimal points. The additional lower resolution cases were also run to confirm the proper convergence of the eigenspectrum. Heavy sponging is applied to avoid the spurious reflections at the outflow boundary. The complex eigenvalue with the largest imaginary part that is least stable one is selected. The two-dimensional mode structure of the

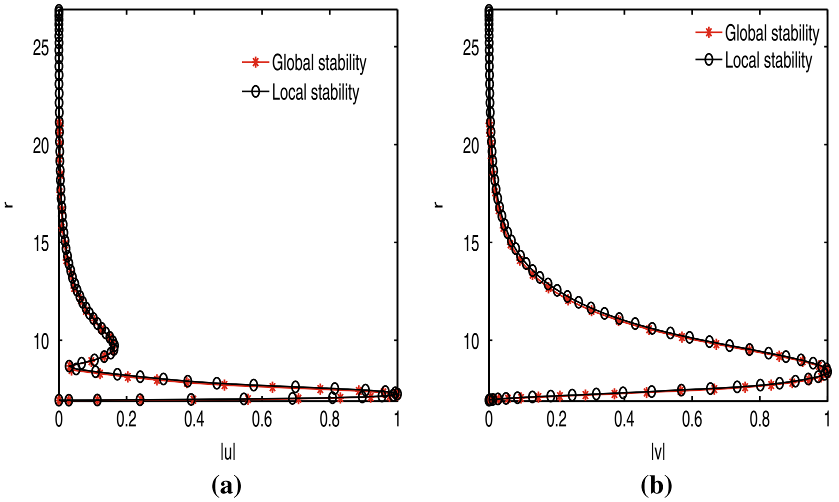

(a) **(b)**

Fig. 12 Comparison of the modulus of eigenfunctions **a** u and **b** v at same streamwise location $x = 262$ for axisymmetric ($N = 0$) computed from global and local approaches at same streamwise location. The associated real frequency is $\omega_r = 0.075$

Table 2 The grid convergence study for two leading eigenvalues ω_1 and ω_2 for $R_e = 383$ and $N = 1$ for different grid size

Mesh	L_x	L_r	$n \times m$	n	m	ω_1	ω_2	Error (%)
#1	345	20	14,641	121	121	$0.03314 - 0.01639i$	$0.02692 - 0.01645i$	3.73
#2	345	20	11,449	107	107	$0.03300 - 0.01580i$	$0.02676 - 0.01587i$	3.99
#3	345	20	8649	93	93	$0.03288 - 0.01520i$	$0.02662 - 0.01526i$	–

The grid refinement ratio in each direction is 1.14. The maximum relative error is shown here

selected modes is also checked for the spurious mode. The real boundary layer profile is used for the stability computations reported here.

6.1 Grid convergence study

A grid convergence study was performed to check the accuracy of the solution and appropriate grid size. Table 2 shows the values of two leading eigenvalues computed for $Re = 383$ for helical mode $N = 1$ mode using three different grid size. The grid resolution was successively improved by a factor of 1.14 in axial and radial directions, respectively. The real and imaginary parts of the eigenvalues show monotonic convergence of the solution with the increased spatial resolution. In this table, n and m indicate the number of grids in axial and radial directions, respectively. The relative errors are calculated between consecutive grids for real and imaginary parts of the eigenvalues. The largest associated error among both the eigenmodes is considered. The relative error for mesh 1 is well within the limit, and it is used for all the results reported here. The domain height $L_r = 20$ is sufficient in wall normal direction to impose free-stream boundary condition [2].

6.2 Pressure boundary condition

Two-dimensional instability analysis in primitive variable approach needs boundary conditions for the unknown pressure disturbances to close the formulation. The pressure compatibility (PC) conditions, derived from the linearized Navier–Stokes equations (Eq. 13) and collocated at the wall, have been used successfully in the instability analysis of incompressible flows [19,20,22,37,38]. However, pressure Poisson equations have been used for pressure boundary conditions for open and closed flows consistent with mass conservation which could be considered to provide addition information than linearized Navier–Stokes equations [29]. We have derived linearized pressure Poisson equation (LPPE) for the pressure perturbations in a similar fashion as [36]. The LPPE is given by,

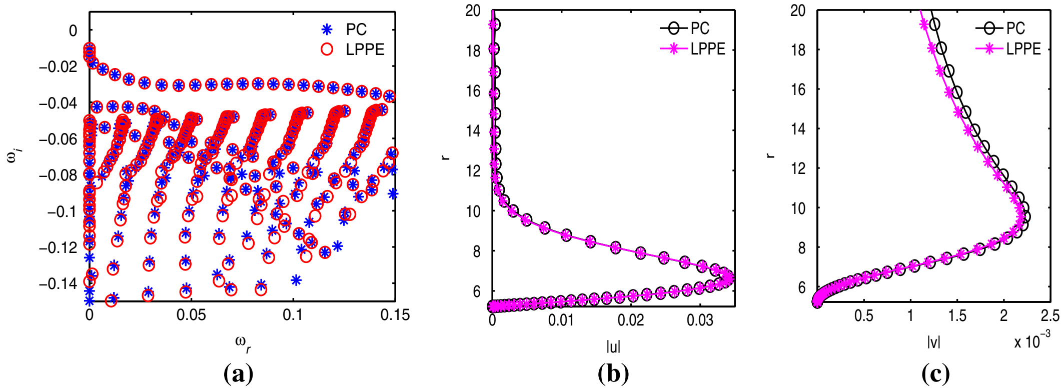

Fig. 13 Comparison of eigenspectrum and eigenfunctions for axisymmetric mode, $N = 0$, $Re = 383$ and $L_x = 345$ for pressure compatibility conditions (PC) and linearized Poisson pressure equations (LPPE)

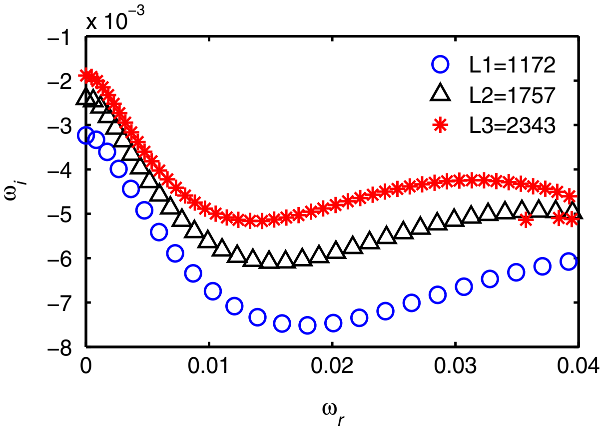

Fig. 14 Eigenspectrum of three different streamwise domain length for $Re = 383$

$$\left(\frac{\partial}{\partial r^2} + \frac{1}{r}\frac{\partial}{\partial r} - \frac{N^2}{r^2} + \frac{\partial}{\partial x^2}\right) p + 2\left(\frac{\partial U}{\partial x}\frac{\partial}{\partial x} + \frac{\partial V}{\partial x}\frac{\partial}{\partial r}\right) u$$
$$+2\left(\frac{\partial U}{\partial r}\frac{\partial}{\partial x} + \frac{\partial V}{\partial r}\frac{\partial}{\partial r} + \frac{2V}{r^2}\right) v + \frac{2V}{r^2} iNw = 0 \quad (31)$$

where N is the azimuthal wave number.

Figure 13a shows the comparison of the spectra for PC and LPPE boundary conditions. The spectra of both the boundary conditions are in good agreement. Figure 13b, c shows that the eigenfunctions u and v are also in good agreement for $Re = 383$. PC boundary condition is used in all global instability results reported here.

6.3 Effect of domain length

Global stability computations of a finite size of the domain need boundary conditions in the streamwise direction. The literature on the global stability of truncated domain shows that the spectra obtained strongly depend on the type and position of boundary conditions applied [1,12]. The temporal growth rate increases with the increased streamwise domain length for same inlet Reynolds number. Figure 14 shows the comparison of the spectrum for three domain length $L_x = 1171$, 1757 and 2343. It shows that the space between the frequencies depends on the domain length truncation. The frequencies are more closer for the larger domain, and ideally it becomes continuous for the infinite domain length. The two-dimensional spatial structure in Fig. 15 shows that the eigenvalues and eigenfunctions are the function of domain length L_x.

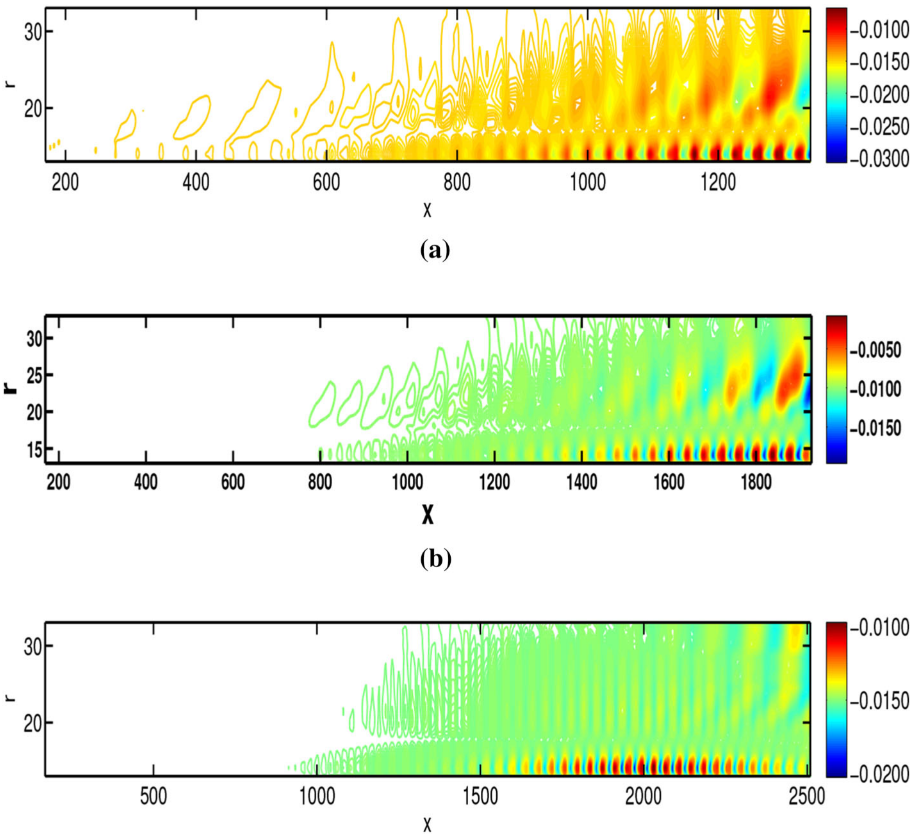

(a)

(b)

(c)

Fig. 15 Contour plot of streamwise disturbance amplitudes u for axisymmetric mode ($N = 0$) and $Re = 383$ for different streamwise domain length and frequency $\omega_r = 0.038$ **a** $L_x = 1172$, **b** $L_x = 1757$ and, **c** $L_x = 2343$

6.4 Axisymmetric mode

Figure 16 shows the eigenspectrum for the axisymmetric mode ($N = 0$) with Reynolds number, $Re = 383$. The global modes of the real boundary layer have larger temporal growth rate compared to the model boundary layer. Thus, the real base flow is globally less stable than that of model boundary layer.

In the above figure, the eigenmodes marked by circle and square are stationary ($\omega_r = 0$) and oscillatory ($\omega_r > 0$) modes, respectively. The stationary mode has a complex frequency $\omega = 0 - 0.009943i$. This global mode is temporally stable because $\omega_i < 0$, and hence, disturbances decay in time. Figure 17 shows the two-dimensional spatial structure of the streamwise (u) and wall normal (v) disturbance amplitudes for stationary mode $\omega = 0 - 0.009943i$. The magnitudes of the velocity disturbances are zero at the inflow boundary, as it is the inlet boundary condition. As the fluid particles move towards the downstream, the disturbances evolve monotonically in time within the domain and progresses towards the downstream. The magnitude of the u disturbance amplitudes is one order higher than that of v disturbance amplitudes. The amplitude structure has opposite sign for u and v. The spatial structure of the amplitudes grows in size and magnitude towards the downstream. Figure 18 shows the variation of u and v disturbance amplitudes in streamwise direction at different radial locations. The magnitude of the disturbance amplitudes is very small near the cylinder surface due to viscous effect, increases in the radial direction and vanishes at far field.

The most unstable oscillatory mode has an eigenvalue $\omega = 0.004363 - 0.01475i$. The flow is stable for this global mode because $\omega_i < 0$. The spatial structure of the above global eigenmode for u and v disturbance amplitudes is not monotonic in nature. The distribution in spatial directions is shown in Fig. 19. The amplitudes of the velocity disturbances are zero at the inlet as it is the imposed boundary condition at the inlet. However, in the streamwise direction the disturbances grow in magnitudes and it contaminates the flow field towards the

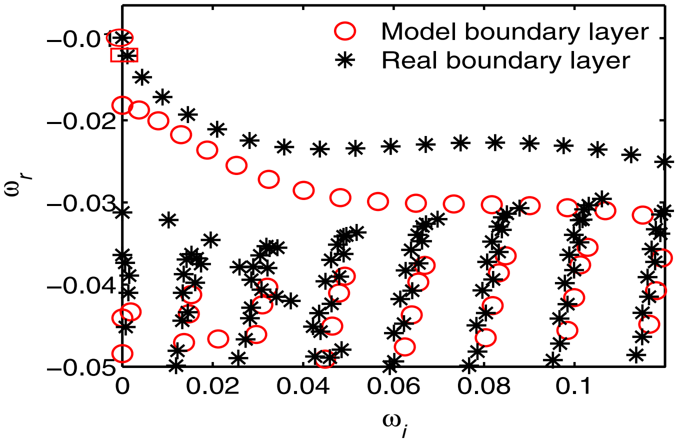

Fig. 16 Eigenspectrum for azimuthal wave number $N = 0$ (axisymmetric mode) and $Re = 383$

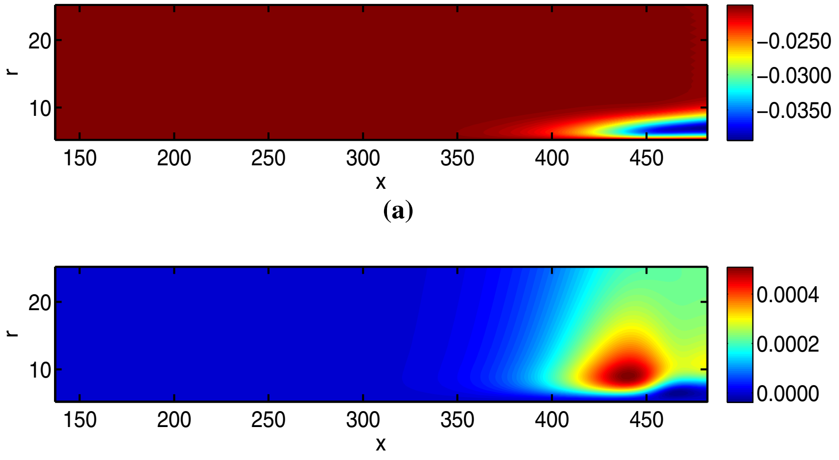

(a)

(b)

Fig. 17 Contour plot of stationary mode **a** streamwise velocity and **b** normal velocity for the eigenvalue $\omega = 0.0 - 0.009943i$, as marked by circle in Fig. 16

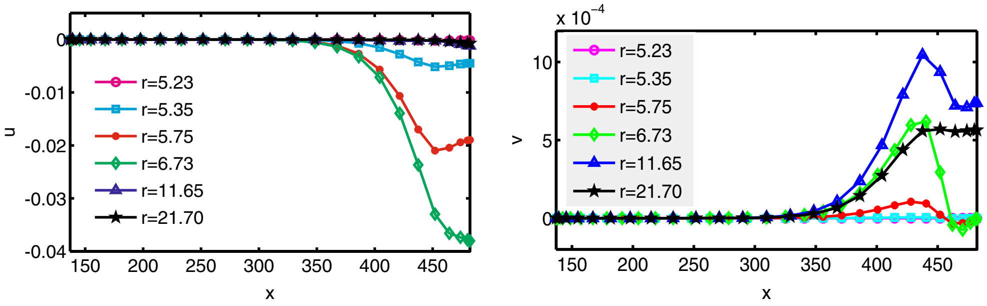

(a) **(b)**

Fig. 18 Variation of disturbance amplitudes in streamwise direction for stationary mode **a** streamwise velocity (u) and **b** normal velocity (v) for the eigenvalue $\omega = 0.0 - 0.009943i$, as marked by circle in Fig. 16

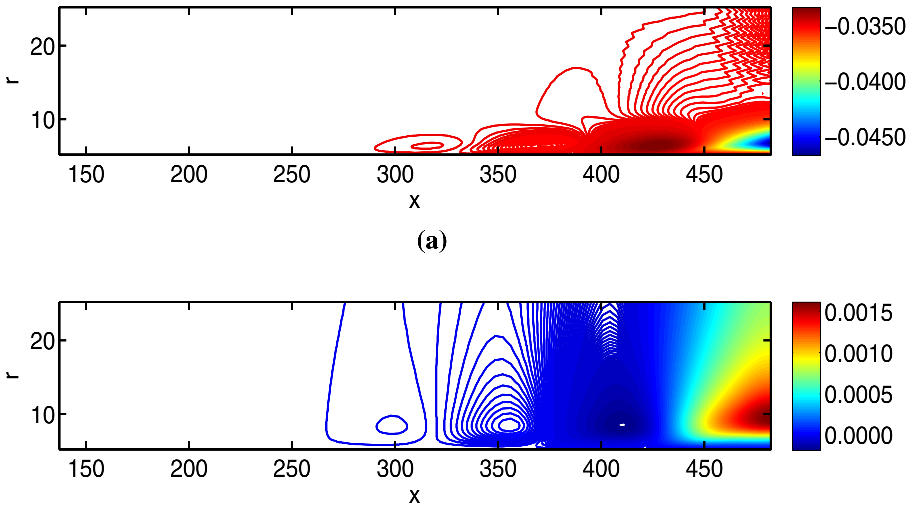

(a)

(b)

Fig. 19 Contour plot of oscillatory mode **a** streamwise velocity and **b** normal velocity for the eigenvalue $\omega = 0.004363-0.01475i$, as marked by square in Fig. 16

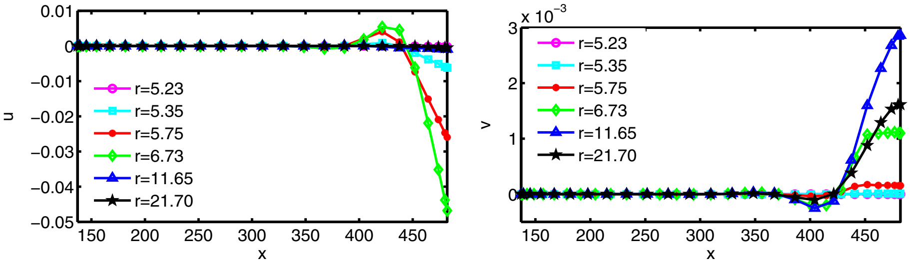

(a) **(b)**

Fig. 20 Variation of disturbance amplitudes in the streamwise direction for oscillatory mode **a** streamwise velocity (u) and **b** normal velocity (v) for the eigenvalue $\omega = 0.004363 - 0.01475i$, as marked by square in Fig. 16

downstream. The magnitudes of the disturbance amplitudes grow exponentially as they move further towards the downstream.

However, its variation in the normal direction is different from that of a stationary mode, as seen in the respective figures. The magnitude of the normal disturbance amplitudes is one order less than that of the streamwise component.

Figure 20 presents variation of disturbance amplitudes in streamwise direction at various radial locations. It shows that the most of the disturbances grow in magnitude as they move towards downstream. The magnitude of the disturbance amplitudes is very small near the wall due to viscous effect, gradually increases in radial direction and finally vanishes at the far field. It shows that disturbances evolve within the flow field in time and grow in magnitude and size while moving towards the downstream.

Figure 21 shows contour plot of the real part of the streamwise disturbance velocity of two different eigenmodes with frequency $\omega_r = 0.021$ & $\omega_r = 0.1125$ for $N = 0$ and $Re = 383$. The streamwise domain length is 345. The disturbances is seen to evolve in the vicinity of the wall and increasing the amplitudes when moving towards downstream. The typical length scale of the wavelet structure decreases with the increases in frequency (ω_r).

6.5 Effect of transverse curvature

The body radius of the cylinder is another important length scale in case of the axisymmetric boundary layer in addition to the boundary layer thickness (δ). The inverse of the body radius is called the transverse surface

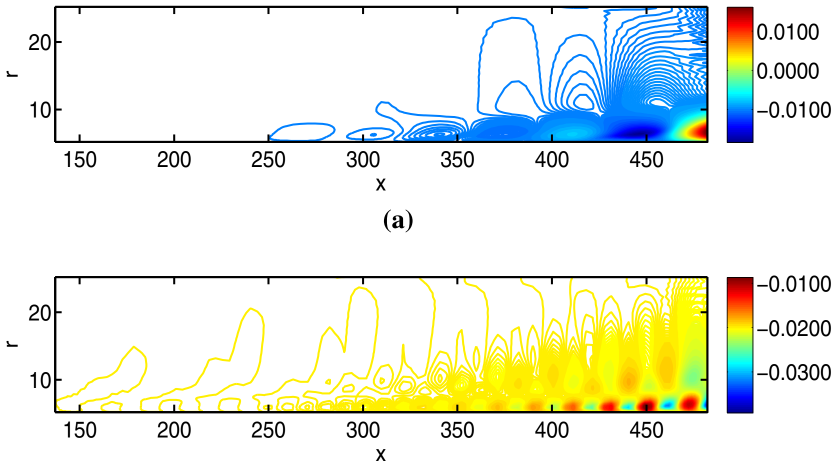

(a)

(b)

Fig. 21 Contour plot of the real part of u for the two different eigenmodes associated with the frequencies **a** $\omega_r = 0.021$ **b** $\omega_r = 0.1125$. The corresponding Reynolds number and azimuthal wave number are $Re = 383$ and $N = 0$, respectively

curvature (S). The flat-plate boundary layer is a special case of a zero transverse curvature. It is normalized with the displacement thickness (δ^*) at the inflow boundary of domain. It has significant effect on the base flow as well as stability characteristics of the axisymmetric boundary layer. In order to understand the transverse curvature effect on the stability characteristic of the axisymmetric boundary layer, the stability characteristics are compared with the flat-plate boundary layer (zero transverse curvature) at the same Reynolds number and domain size. The Reynolds number is computed based on the displacement thickness and free-stream velocity at the inflow boundary. The comparison of spectra, spatial growth rate and spatial eigenfunction for real axisymmetric, model axisymmetric and flat-plate boundary layer is done at the same Reynolds number. Figure 22 shows the comparison of eigenspectrum for three different Reynolds numbers 383, 557 and 909 (based on the body radius of the cylinder, these are 2000, 4000 and 10,000) with $L_x = 345$ for axisymmetric and flat-plate boundary layer. The comparison is limited for the discrete part of the spectrum only. It has been observed that at small Reynolds number the temporal growth rate ω_i is higher for flat-plate boundary than that of axisymmetric boundary layer. The temporal growth rate of real axisymmetric boundary layer is found higher than that of model axisymmetric boundary layer. The difference in the temporal growth rate of the eigenmodes for axisymmetric and flat-plate boundary layer reduces with the increased Reynolds number. The eigenmodes of axisymmetric boundary layer approach eigenmodes of flat-plate boundary layer at higher Reynolds number. This is primarily due to the effect of transverse curvature only. Thus, the transverse curvature has significant damping effect on the disturbances at low Reynolds number. At higher Reynolds number, i.e. $Re = 909$ the spectra are nearly similar for all the three boundary layers. Figure 23 shows the comparison of the spatial amplification rates (A_x) for three different Reynolds numbers for flat-plate and real axisymmetric boundary layer. The least stable eigenmodes have been selected to compute the spatial amplification rate. The comparison shows that at low Reynolds number, A_x is higher for flat-plate boundary layer. It is also observed that the difference in the magnitude of the A_x reduces with the increase in the Reynolds number for both the boundary layers. This damping effect is due to the reduced effect of the transverse curvature at higher Reynolds number.

Three different families of the eigenspectrum are shown for $Re = 383$ in Fig. 24 for real axisymmetric, model axis symmetric and flat-plate boundary layer. The discrete part of the spectrum is only shown in the above figures for the comparison purpose. The difference between the spectrum depends on the domain length. The distance between two consecutive frequencies reduces with the increased domain length. To quantify this discretization of the eigenmodes for $Re = 383$, different domain lengths were considered with $L_{x1} = 345$, $L_{x2} = 475$ and $L_{x3} = 605$. The temporal growth rate increases for a given Reynolds number with larger domain length. Figure 25 shows the comparison of the streamwise (u) and wall normal (v) disturbance amplitudes for $Re = 383$ at streamwise location $x = 300$. The magnitudes of disturbance amplitudes are higher for flat-plate boundary layer.

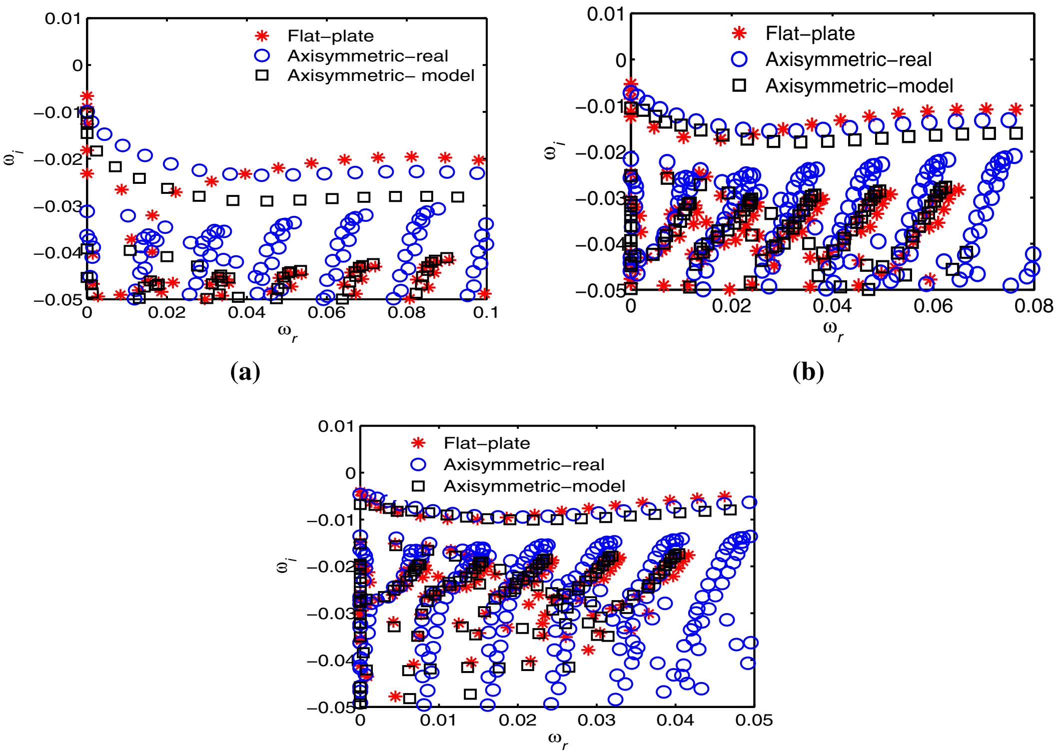

(a) **(b)**

(c)

Fig. 22 Comparison of the eigenspectrum of real axisymmetric, model axisymmetric ($N = 0$), and 2D flat-plate ($\beta = 0$) boundary layer for $L_x = 345$ for three different Reynolds numbers **a** $Re = 383$, **b** $Re = 557$ and **c** $Re = 909$

6.6 Helical modes ($N = 1, 2, 3$)

The spectra for helical modes $N = 1$, 2 and 3 are shown in Fig. 26 for $Re = 383$. The helical mode $N = 1$ is found least stable, and $N = 3$ is found most stable mode. The contour plot of the real part of u disturbance velocity is shown for $N = 1$, 2, and 3 for same frequency $\omega_r = 0.03$. The contour plots shows that the disturbance amplitudes are growing at the outflow boundary for $N = 1$. For $N = 2$ and 3 the disturbance amplitudes starts to amplify at early stage and decaying while leaving the domain at outlet. As the helical mode number increases, the magnitude of amplitudes also increases. Qualitatively the spatial structure are similar for all the three helical modes.

6.7 Temporal growth rate

Figure 28 shows the temporal growth rate of the eigenmodes for different Reynolds numbers. The growth rate increases with the increase in Reynolds number for all the azimuthal wave numbers. As the largest imaginary part is negative for different Reynolds numbers, the flow is temporally stable. The transverse curvature varies inversely with the Reynolds number. At low Reynolds number, growth rate is small and with the increase in Reynolds number growth rate increases. This proves that transverse curvature has significant damping effect on the global temporal mode also. Global modes with higher wave numbers, $N = 3$, 4 and 5 are more stable than axisymmetric and helical modes $N = 1$ and 2. At low Reynolds number, axisymmetric mode is having higher growth rate than that of $N = 1$ and 2. As Reynolds number increases, the growth rate of helical mode $N = 1$ and 2 increases than that of axisymmetric mode.

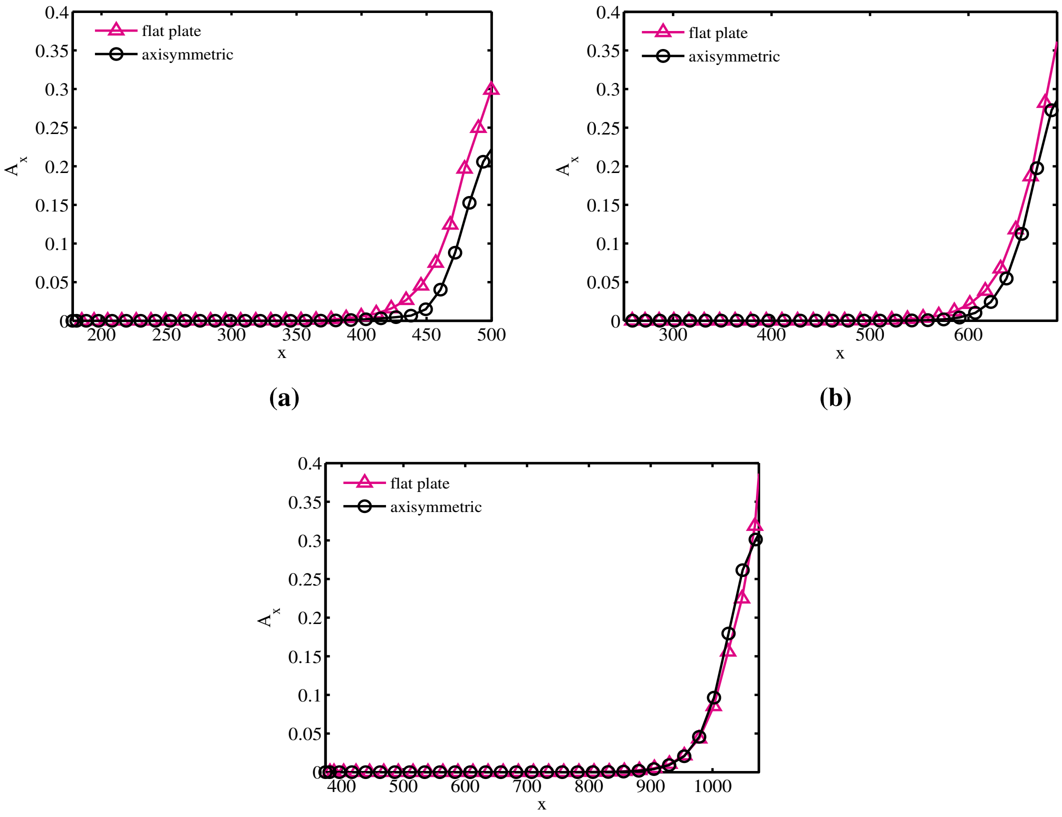

(a)

(b)

(c)

Fig. 23 Comparison of spatial amplification rate of axisymmetric ($N = 0$) and 2D flat-plate ($\beta = 0$) boundary layer for three different Reynolds numbers **a** $Re = 383$, **b** $Re = 557$ and **c** $Re = 909$

6.8 Spatial amplification rate

The global temporal modes exhibit spatial growth or decay in streamwise direction when moving towards the downstream. The disturbances in the streamwise direction at a particular radial location may decay or amplify. However, the overall effect of all disturbances together at each streamwise location can be quantified by computing the spatial amplitude growth, $A(x)$ [12].

$$A(x) = \sqrt{\int_{1}^{r_{max}} (u^{*}(x,r)u(x,r) + v^{*}(x,r)v(x,r) + w^{*}(x,r)w(x,r))\mathrm{d}r} \tag{32}$$

where * denotes the complex conjugate. Figure 29 shows the spatial amplitude growth of the disturbance waves for different azimuthal wave numbers at various Reynolds number. Most unstable oscillatory ($\omega_r \neq 0$) temporal modes are considered to compute the spatial growth of the amplitudes. The growth of the disturbance amplitudes increases in the streamwise direction which makes the flow unstable.

7 Summary

Global stability analysis of axisymmetric boundary layer forms over a circular cylinder is performed by computing global temporal modes using linear stability theory. The numerical eigenvalue problem is solved using ARPACK, which employs Arnoldi's iterative algorithm. The stability analysis is conducted for various Reynolds number and azimuthal wave numbers. The obtained solution of two-dimensional eigenvalues problem and presented results strongly depend on the streamwise extent of the computational domain. The largest imaginary part of the computed eigenvalues is negative for the range of Reynolds number and azimuthal wave

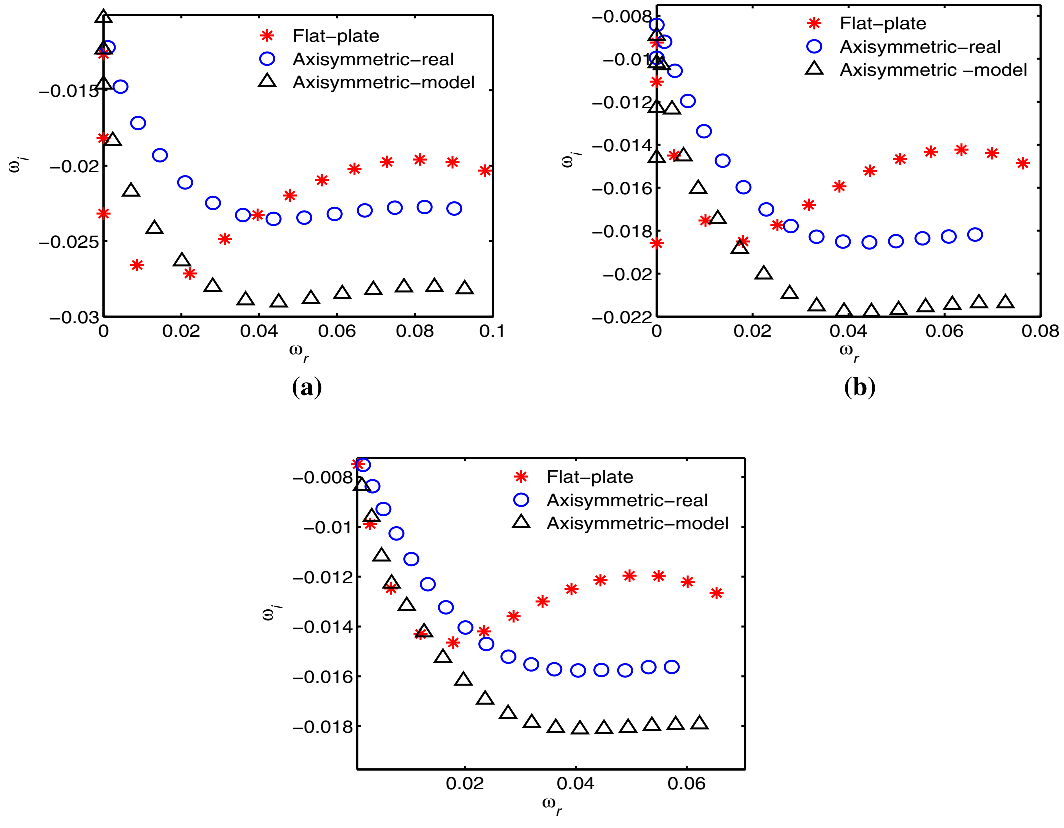

(a) **(b)**

(c)

Fig. 24 Comparison of the eigenspectrum for different streamwise domain lengths **a** $L_x = 345$, **b** $L_x = 475$ and **c** $L_x = 605$ for $Re = 383$ for real axisymmetric, model axisymmetric ($N = 0$) and 2D flat-plate boundary layer ($\beta = 0$)

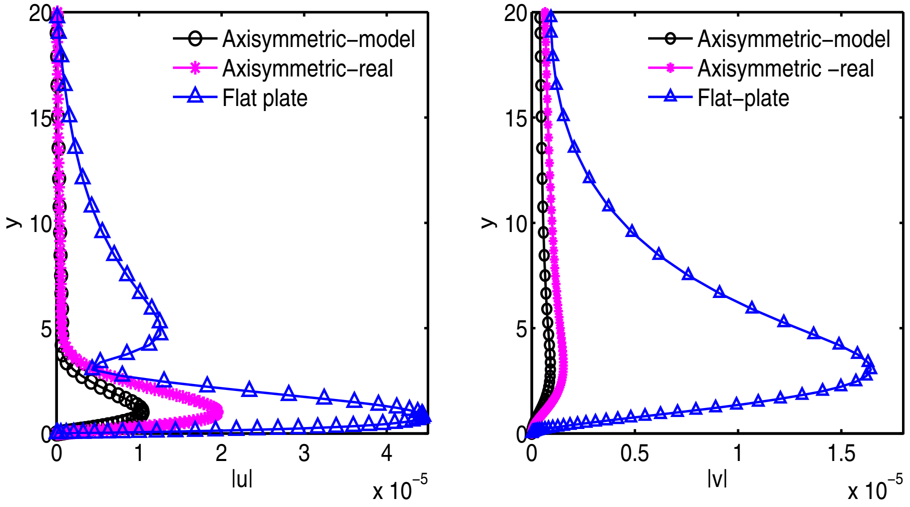

(a) **(b)**

Fig. 25 Comparison of the modulus of eigenfunction **a** u and **b** v at streamwise location $x = 300$ and $Re = 383$ for axisymmetric ($N = 0$) and 2D flat-plate boundary layer ($\beta = 0$). The eigenmode selected for flat-plate and axisymmetric boundary layer is least stable temporal mode. The associated eigenvalues are $\omega = 0.08121 - 0.01959i$ (flat plate) and $\omega = 0.005742 - 0.02436$ (axisymmetric) boundary layer

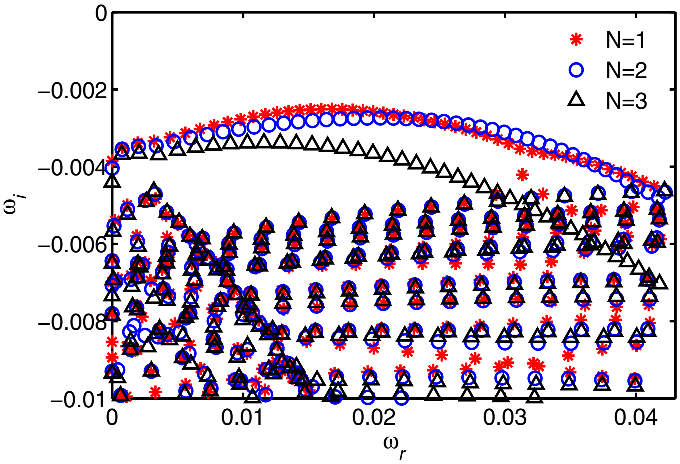

Fig. 26 Comparison of the eigenspectrum for $Re = 383$ and azimuthal wave numbers $N = 1$, 2 and 3

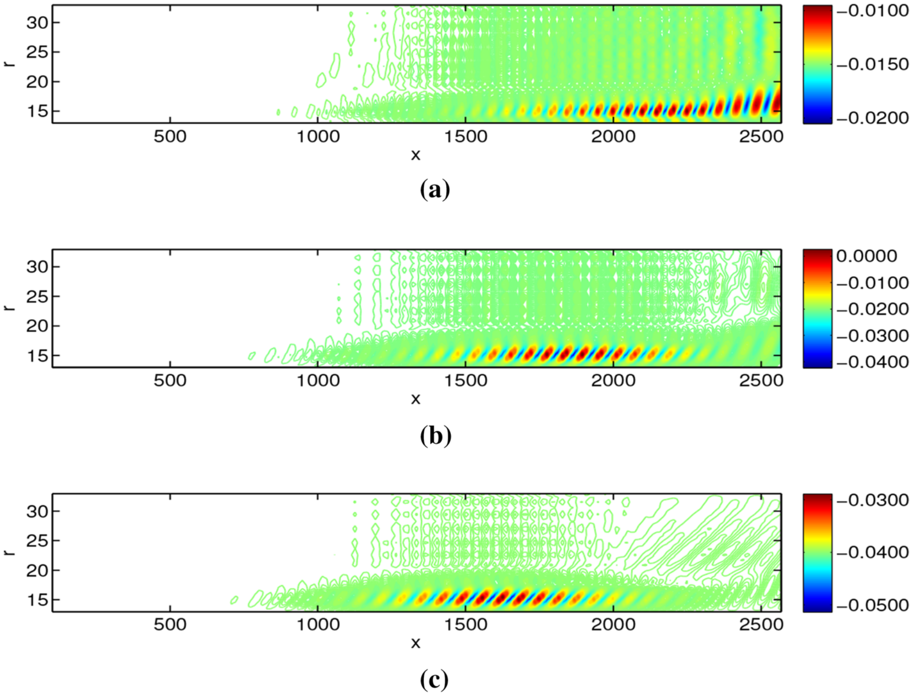

Fig. 27 Contour plot of real parts of disturbance amplitudes u for $Re = 383$ and $\omega_r = 0.03$ **a** $N = 1$, **b** $N = 2$, **c** $N = 3$

numbers considered here for real and model axisymmetric boundary layers. Thus, the flow is temporally stable. The global modes in axisymmetric boundary layer showed wave-like behaviour for the range of Reynolds numbers considered. The spatial properties of the global modes show that the disturbances grow in size and magnitude within the flow domain in the streamwise direction when moving towards the downstream. The global modes of the real axisymmetric boundary layer are found less stable than those of model boundary layer. The axisymmetric mode ($N = 0$) is found the least stable one for the range of Reynolds number considered here. The helical mode $N = 1$ is less stable than $N = 2$ at lower Reynolds number, while $N = 2$ is less stable than $N = 1$ at higher Reynolds number. The global modes of higher azimuthal wave numbers, $N = 3$, 4 and 5, are found more stable. The temporal global modes of axisymmetric boundary layer are found more stable than that of flat-plate boundary layer at the same Reynolds number. Thus, the temporal growth rate ω_i is smaller for axisymmetric boundary layer. However, this effect is found significant at smaller Reynolds number. As the Reynolds number increased, the temporal growth rate of axisymmetric modes also increased

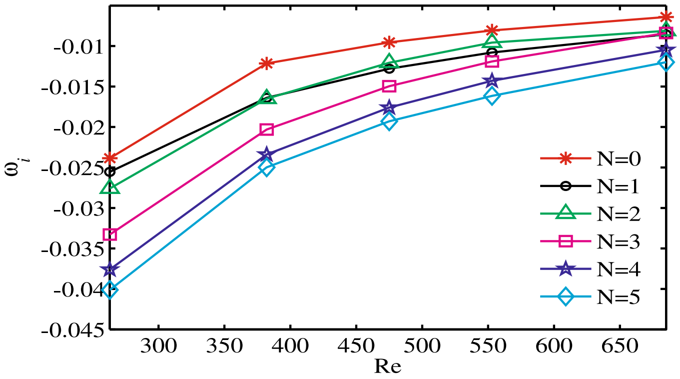

Fig. 28 Variation of the temporal growth rate (ω_i) with the Reynolds number for different azimuthal wave numbers (N)

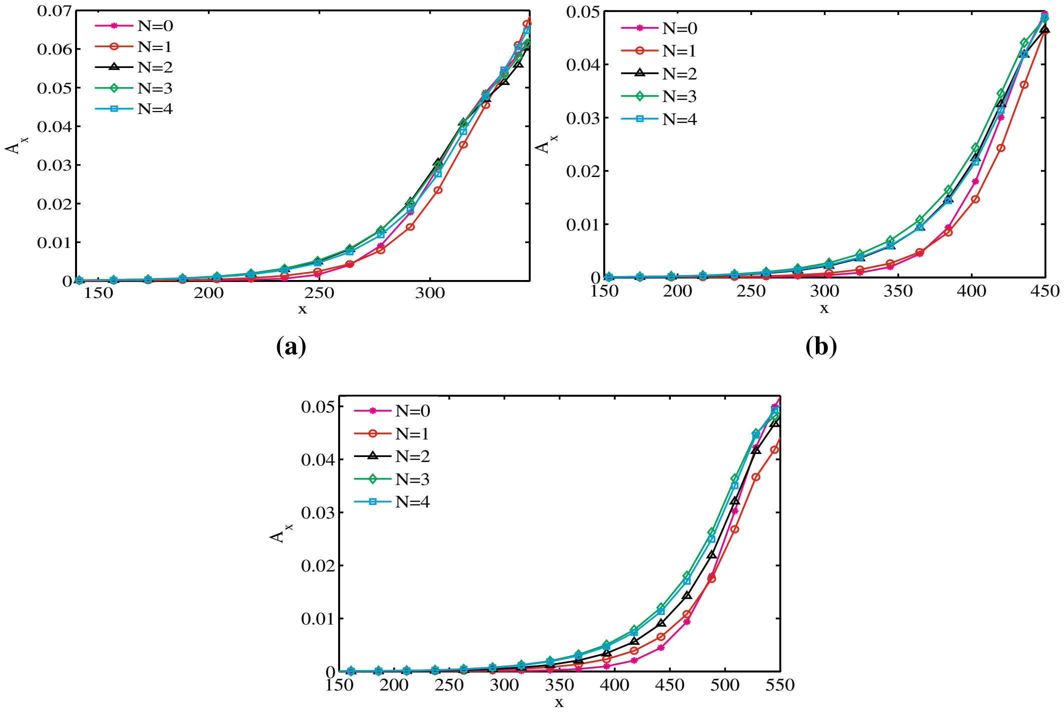

(a)

(b)

(c)

Fig. 29 Spatial amplification rate A_x in streamwise direction x for **a** $Re = 383$, **b** $Re = 557$ and **c** $Re = 685$ for different azimuthal wave numbers. The most unstable temporal mode is considered to compute the spatial amplitude growth A_x

and approached 2D modes of flat-plate boundary layer. Thus, at low Reynolds number the effect of transverse curvature is significant. The transverse curvature reduces with the increased Reynolds number, and global modes become less stable. Thus, the transverse curvature shows overall damping effect on the global modes. The amplitude functions corresponding to the stationary mode are found to be monotonically growing in the streamwise direction.

Acknowledgements The authors acknowledge the constructive suggestions by the anonymous reviewer. The discussions with Prof. R. Govindarajan and Dr. G. Swaminathan during the work and manuscript preparation is sincerely acknowledged. The authors also wish to express gratitude for the finanical support by Aeronautical Research and Development Board (AR&DB), India.

References

1. Akervik, E., Ehrenstein, U., Gallaire, F., Henningson, D.S.: Global two-dimensional stability measure of the flat plate boundary-layer flow. Eur. J. Mech. B/Fluids **27**, 501–513 (2008)
2. Alizard, F., Robinet, J.C.: Spatially convective global modes in a boundary layer. Phys. Fluids **19**, 114105 (2007)
3. Bert, P.: Universal short wave instability of two dimensional eddies in inviscid fluid. Phys. Rev. Lett. **57**, 2157–2159 (1986)
4. Christodoulou, K.N., Scriven, L.E.: Finding leading modes of a viscous free surface flow: an asymmetric generalized eigenproblem. J. Sci. Comput. **3**, 355–406 (1988)
5. Costa, B., Don, W., Simas, A.: Spatial resolution properties of mapped spectral Chebyshev methods. In: Proceedings SCPDE: Recent Progress in Scientific Computing, pp. 179–188 (2007)
6. Crighton, D.G., Gaster, M.: Stability of slowly diverging jet flow. J. Fluid Mech. **77**, 397–413 (1976)
7. Drazin, P.G., Reid, W.H.: Hydrodynamic Stability. Cambridge Univerisity Press, Cambridge (2004)
8. Duck, P.W.: The effect of a surface discontinuity on an axisymmetric on an axisymmetric boundary layer. Q. J. Mech. Appl. Math. **37**, 57–74 (1984)
9. Duck, P.W.: The inviscid axisymmetric stability of the supersonic flow along a circular cylinder. J. Fluid Mech. **214**, 611–637 (1990)
10. Duck, P.W., Hall, P.: On the interaction of Tollmien-Schlichting waves in axisymmetric supersonic flows. Q. J. Mech. Appl. Math. **42**, 115–130 (1989)
11. Duck, P.W., Shaw, S.J.: The inviscid stability of supersonic flow past a sharp cone. Theor. Comput. Fluid Dyn. **2**, 139–163 (1990)
12. Ehrenstein, U., Gallaire, F.: On two-dimensional temporal modes in spatially evolving open flow: the flat-plate boundary layer. J. Fluid Mech. **536**, 209–218 (2005)
13. Fasel, H., Rist, U., Konzelmann, U.: Numericla investigation of the three-dimensional development in boundary layer transition. AIAA J. **28**, 29–37 (1990)
14. Glauert, M.B., Lighthill, M.J.: The axisymmetric boundary layer on a thin cylinder. Proc. R. Soc. A **230**, 1881 (1955)
15. Herrada, M.A., Del Pino, C., FernandezFeria, R.: Stability of the boundary layer flow on a long thin rotating cylinder. Phys. Fluids **20**, 034105 (2008)
16. Jackson, C.P.: A finite-element study of the onset of vortex shedding in flow past variously shaped bodies. J. Fluid Mech. **182**, 2345 (1987)
17. Joseph, D.D.: Nonlinear stability of the Boussinesq equations by the method of energy. Arch. Ration. Mech. **22**, 163–184 (1966)
18. Kao, K., Chow, C.: Stability of the boundary layer on a spinning semi-infinite circular cylinder. J. Spacecr. Rockets **28**, 284–291 (1991)
19. Lin, R.S., Malik, M.R.: On the stability of attachment-line boundary layers. Part 1. The incompressible swept Hiemenz flow. J. Fluid Mech. **311**, 239–255 (1996)
20. Lin, R.S., Malik, M.R.: On the stability of attachment-line boundary layers. Part 2. The incompressible swept Hiemenz flow. J. Fluid Mech. **333**, 125–137 (1997)
21. Mack, L.M.: Stability of axisymmetric boundary layers on sharp cones at hypersonic mach numbers. In: 19th AIAA, Fluid Dynamics, Plasma Dynamics, and Lasers Conference, p. 1413 (1987)
22. Malik, M.R.: Numerical methods for hypersonic boundary layer stability. J. Comput. Phys. **86**, 376–412 (1990)
23. Malik, M.R., Poll, D.I.A.: Effect of curvature on three dimensional boundary layer stability. AIAA J. **23**, 1362–1369 (1985)
24. Malik, M.R., Spall, R.E.: On the stability of compressible flow past axisymmetric bodies. J. Fluid Mech. **228**, 443–463 (1987)
25. Monokrousos, A., Akervik, E., Brandt, L., Heningson, H.: Global three-dimensional optimal disturbances in the Blasius boundary layer flow using time steppers. J. Fluid Mech. **650**, 181–214 (2010)
26. Muralidhar, S.D., Pier, B., Scott, J.F., Govindarajan, R.: Flow around a rotating, semi-infinite cylinder in an axial stream. Proc. R. Soc. A **472**, 20150850 (2016)
27. Petrov, G.V.: Boundary layer on rotating cylinder in axial flow. J. Appl. Mech. Tech. Phys. **17**, 506–510 (1976)
28. Rao, G.N.V.: Mechanics of transition in an axisymmetric laminar boundary layer on a circular cylinder. J. Appl. Math. Phys. **25**, 6375 (1974)
29. Rempfer, D.: On boundary conditions for incompressible Navier–Stokes problems. App. Mech. Rev. **59**(3), 107–125 (2006)
30. Roache, P.J.: A method for uniform reporting of grid refinement study. J. Fluids Eng. **116**, 405413 (1994)
31. Swaminathan, G., Shahu, K., Sameen, A., Govindarajan, R.: Global instabilities in diverging channel flows. Theor. Comput. Fluid Dyn. **25**, 53–64 (2011)
32. Tatsumi, T., Yoshimura, T.: Stability of the laminar flow in a rectangular duct. J. Fluid Mech. **212**, 437–449 (1990)
33. Tezuka, A., Suzuki, K.: Three-dimensional global linear stability analysis of flow around a spheroid. AIAA J. **44**, 1697–1708 (2006)
34. Theofilis, V.: Advances in global linear instability analysis of nonparallel and three dimensional flows. Prog. Aerosp. Sci. **39**, 249315 (2003)
35. Theofilis, V.: Global linear instability. Annu. Rev. Fluid Mech. **43**, 319–352 (2011)
36. Theofilis, V.: The linearized pressure Poisson equation for global instability analysis of incompressible flows. Theor. Comput. Fluid Dyn. **31**, 623–642 (2017)
37. Theofilis, V., Duck, P.W., Owen, J.: Viscous linear stability analysis of rectangular duct and cavity flows. J. Fluid Mech. **505**, 249–286 (2004)
38. Theofilis, V., Fedorov, A., Obrist, D., Dallman, U.C.: The extended Görtler–Hämmerlin model for linear instability of three-dimensional incompressible swept attachment-line boundary layer flow. J. Fluid Mech. **487**, 271–313 (2003)
39. Theofilis, V., Stefan, H., Dallmann, U.: On the origins of unsteadiness and three dimensionality in a laminar separation bubble. Proc. R. Soc. A **358**, 1777 (2000)
40. Tutty, O.R., Price, W.G.: Boundary layer flow on a long thin cylinder. Phys. Fluids **14**, 628–637 (2002)

41. Vinod, N.: Stability and transition in boundary layers: effect of transverse curvature and pressure gradient. Ph.D. Thesis, Jawaharlal Nehru Center for Advanced Scientific Research (2005)
42. Vinod, N., Govindarajan, R.: Secondary instabilities in incompressible axisymmetric boundary layers: effect of transverse curvature. J. Fliud Eng. **134**, 024503 (2012)
43. Zebib, A.: Stability of viscous flow past a circular cylinder. J. Eng. Math. **21**, 155–165 (1987)